K^- nuclear potentials from in-medium chirally motivated models

A. Cieplý,[1,*] E. Friedman,[2,†] A. Gal,[2,‡] D. Gazda,[1,§] and J. Mareš[1,‖]

[1]*Nuclear Physics Institute, 25068 Řež, Czech Republic*
[2]*Racah Institute of Physics, The Hebrew University, Jerusalem 91904, Israel*

A self-consistent scheme for constructing K^- nuclear optical potentials from subthreshold in-medium $\bar{K}N$ s-wave scattering amplitudes is presented and applied to analysis of kaonic atoms data and to calculations of K^- quasibound nuclear states. The amplitudes are taken from a chirally motivated meson-baryon coupled-channel model, both at the Tomozawa-Weinberg leading order and at the next to leading order. Typical kaonic atoms potentials are characterized by a real part $-\text{Re}\, V_{K^-}^{\text{chiral}} = 85 \pm 5$ MeV at nuclear matter density, in contrast to half this depth obtained in some derivations based on in-medium $\bar{K}N$ threshold amplitudes. The moderate agreement with data is much improved by adding complex ρ- and ρ^2-dependent phenomenological terms, found to be dominated by ρ^2 contributions that could represent $\bar{K}NN \to YN$ absorption and dispersion, outside the scope of meson-baryon chiral models. Depths of the real potentials are then near 180 MeV. The effects of p-wave interactions are studied and found secondary to those of the dominant s-wave contributions. The in-medium dynamics of the coupled-channel model is discussed and systematic studies of K^- quasibound nuclear states are presented.

I. INTRODUCTION

A key issue in studying in-medium K^- meson interactions concerns the strength of the attractive K^- nuclear potential [1]. Related topical questions involve (i) the underlying free-space $\bar{K}N$ interaction and whether or not it can realistically support K^- nuclear clusters (see Ref. [2] for a recent review), and (ii) the role of K^- mesons in multistrange self-bound matter [3] and in compact stars [4]. An order of magnitude estimate of the nuclear potential V_{K^-} is provided by the leading-order (LO) Tomozawa-Weinberg (TW) vector term of the chiral effective meson-baryon Lagrangian [5] which in the Born approximation gives

$$V_{K^-} = -\frac{3}{8f_\pi^2}\rho \approx -57\frac{\rho}{\rho_0} \quad \text{(in MeV)}, \quad (1)$$

where ρ is the nuclear density, $\rho_0 = 0.17$ fm^{-3}, and $f_\pi \approx 93$ MeV is the pion decay constant. This attraction is doubled, roughly, within chirally based coupled-channel $\bar{K}N$–$\pi\Sigma$–$\pi\Lambda$ calculations that produce dynamically a $\bar{K}N$ quasibound state loosely identified with the $\Lambda(1405)$ resonance [6]. Deeper potentials, in the range Re $V_{K^-}(\rho_0) \sim -(150$–$200)$ MeV are obtained in comprehensive global fits to K^--atom strong-interaction shifts and widths by introducing empirical density dependent effective K^-N amplitudes [7–10]. Such strongly attractive potentials are expected to generate K^- nuclear quasibound states which could prove relatively narrow once the strong transition $\bar{K}N \to \pi\Sigma$ becomes kinematically forbidden for binding energies exceeding about 100 MeV,

as conjectured by Akaishi and Yamazaki [11]. Experimentally, we mention the K^- quasibound signals claimed for K^-pp [12,13] at and below the $\pi\Sigma N$ threshold. However, these reported signals are quite broad, at variance with the underlying physics. In contrast to the indications of a deep K^- potential, considerably shallower potentials, Re $V_{K^-}(\rho_0) \sim -(40$–$60)$ MeV, are obtained for zero kinetic-energy kaons by introducing self-energy (SE) contributions to the in-medium K^-N threshold scattering amplitude, within a self-consistent procedure that includes in particular the potential V_{K^-} thus generated [14,15].

In a recent Letter [16] we reported on new, self-consistent calculations of K^- quasibound states that lead to deep K^- nuclear potentials, considerably deeper than the "shallow" potentials deduced in Refs. [14,15]. The basic idea is to identify the K^-N *subthreshold* energy domain required for the construction of V_{K^-}. For kaonic atoms, essentially at the K^- nuclear threshold, this was explored during the 1970s by Wycech [17], Bardeen and Torigoe [18], and Rook [19] who noted the dominance of the subthreshold $\bar{K}N$ quasibound state $\Lambda(1405)$ in causing the in-medium $\bar{K}N$ scattering amplitude to become more attractive as one goes to subthreshold K^-N energies. In our Letter [16] we applied this idea, introducing a new self-consistency requirement, to a comprehensive study of kaonic atoms that uses scattering amplitudes derived from a chirally motivated coupled channel meson-baryon Lagrangian [20]. Here we expand on these recent calculations to provide more details on derivation, systematics and results. In addition to the next to leading-order (NLO) model CS30 used in the Letter, in the present work we report on a new LO model TW1 fitted to the new SIDDHARTA values of shift and width of the $1s$ state in the K^- hydrogen atom [21].

The paper is organized as follows. In Sec. II we describe a self-consistent scheme of handling in-medium subthreshold K^-N scattering amplitudes used in the construction of V_{K^-}. In Sec. III we discuss the derivation of in-medium scattering

*cieply@ujf.cas.cz
†elifried@vms.huji.ac.il
‡avragal@vms.huji.ac.il
§gazda@ujf.cas.cz
‖mares@ujf.cas.cz

amplitudes in both models TW1 and CS30. Some details are relegated to an appendix. In Sec. IV we discuss kaonic atom calculations, and in Sec. V we discuss calculations of K^- nuclear quasibound states. Section VI concludes the work with a brief summary of the main results.

II. HANDLING $K^- N$ SUBTHRESHOLD AMPLITUDES

In the single-nucleon approximation, the K^- potential in nuclear matter of density ρ is given in terms of the in-medium $K^- N$ scattering amplitude $F_{K^- N}$,

$$V_{K^-} = -\frac{2\pi}{\omega_K}\left(1+\frac{\omega_K}{m_N}\right)F_{K^- N}(\vec{p}, \sqrt{s}; \rho)\,\rho, \qquad (2)$$

where $F_{K^- N}(\vec{p}, \sqrt{s}; \rho \to 0)$ reduces to the free-space two-body $K^- N$ c.m. forward scattering amplitude $F_{K^- N}(\vec{p}, \sqrt{s})$ and the nucleon energy E_N is approximated by its mass m_N in the kinematical factor in front of $F_{K^- N}$. Here, $\vec{p}$ is the relative $K^- N$ momentum and $s = (E_K + E_N)^2 - (\vec{p}_K + \vec{p}_N)^2$ is the Lorentz invariant Mandelstam variable s which reduces to the square of the total $K^- N$ energy in the two-body c.m. frame. In the laboratory frame, $E_K = \omega_K$. Before constructing V_{K^-} for use in actual calculations, we need to prescribe how to interpret in Eq. (2) the two-body arguments $\vec{p}$ and $\sqrt{s}$ of the in-medium scattering amplitude. For s-wave amplitudes, the momentum dependence arises through the magnitude p of the relative momentum $\vec{p}$ which near threshold is approximated by

$$\vec{p} = \xi_N \vec{p}_K - \xi_K \vec{p}_N, \quad \xi_{N(K)} = m_{N(K)}/(m_N + m_K). \quad (3)$$

Averaging over angles, the square of $\vec{p}$ assumes the form

$$p^2 \to \xi_N \xi_K \left(2m_K \frac{p_N^2}{2m_N} + 2m_N \frac{p_K^2}{2m_K}\right). \qquad (4)$$

For $\sqrt{s}$ we note that $\vec{p}_K + \vec{p}_N = 0$ in the two-body c.m. system, but $\vec{p}_K + \vec{p}_N \neq 0$ in the nuclear laboratory system which nearly coincides with the K^--nucleus c.m. system. Averaging over angles yields $(\vec{p}_K + \vec{p}_N)^2 \to (p_K^2 + p_N^2)$. Near threshold, neglecting quadratic terms in the binding energies $B_K = m_K - E_K$, $B_N = m_N - E_N$, we have

$$\sqrt{s} \approx E_{\text{th}} - B_N - B_K - \xi_N \frac{p_N^2}{2m_N} - \xi_K \frac{p_K^2}{2m_K}, \qquad (5)$$

where $E_{\text{th}} = m_N + m_K$. To transform the momentum dependence into density dependence, the nucleon kinetic energy $p_N^2/(2m_N)$ is approximated in the Fermi gas model by $T_N(\rho/\rho_0)^{2/3}$, with $T_N = 23.0$ MeV, and the K^- kinetic energy $p_K^2/(2m_K)$ is identified in the local density approximation with $-B_K - \text{Re}\,\mathcal{V}_{K^-}(\rho)$, where $\mathcal{V}_{K^-} = V_{K^-} + V_c$ and V_c is the K^- finite-size Coulomb potential. Under these approximations, Eqs. (4) and (5) become

$$p^2 \approx \xi_N \xi_K [2m_K T_N(\rho/\rho_0)^{2/3} - 2m_N(B_K + \text{Re}\,\mathcal{V}_{K^-}(\rho))], \qquad (6)$$

where both terms on the r.h.s. are positive for attractive V_{K^-}, and

$$\sqrt{s} \approx E_{\text{th}} - B_N - \xi_N B_K - 15.1\left(\frac{\rho}{\rho_0}\right)^{2/3} + \xi_K \text{Re}\,\mathcal{V}_{K^-}(\rho), \qquad (7)$$

where *all* the terms following E_{th} on the r.h.s. are negative, thus implementing the anticipated downward energy shift into the $K^- N$ subthreshold energy region. Equation (7) is used in most of the bound state applications below as is, although we also checked the effect of implementing gauge invariance through the substitution $\sqrt{s} \to \sqrt{s} - V_c$. Gauge invariance often is not implemented in the solution of the free-space Lippmann-Schwinger equations of underlying chiral models simply because its effects on the two-body meson-baryon system are negligible.

We note that the K^- nuclear potential V_{K^-} appears as an argument in expressions (6) and (7) for p^2 and $\sqrt{s}$, respectively, which in turn serve as arguments in expression (2) for this same V_{K^-}. This suggests to calculate V_{K^-} self-consistently within a scheme in which the downward energy shift into the $K^- N$ subthreshold energy region is density dependent and is controlled by the outcome self-consistent $V_{K^-}(\rho)$. In the corresponding sections below we elaborate on the self consistency scheme which is applied to the solution of the wave equation satisfied by in-medium K^- mesons.

III. IN-MEDIUM $\bar{K}N$ AMPLITUDES

The synergy of chiral perturbation theory and coupled channel T-matrix resummation techniques provides successful description of $\bar{K}N$ interactions at low energies [2]. In our approach we employ chirally motivated coupled-channel s-wave potentials that are taken in a separable form,

$$V_{ij}(p, p'; \sqrt{s}) = \sqrt{\frac{1}{2\omega_i}\frac{M_i}{E_i}}\,g_i(p)\,\frac{C_{ij}(\sqrt{s})}{f_\pi^2}\,g_j(p')\sqrt{\frac{1}{2\omega_j}\frac{M_j}{E_j}},$$

$$g_j(p) = \frac{1}{1 + (p/\alpha_j)^2}, \qquad (8)$$

with E_i, M_i, and ω_i denoting baryon energy, baryon mass, and meson energy in the c.m. system of channel i. The coupling matrix C_{ij} is determined by chiral SU(3) symmetry. The parameter $f_\pi \sim 100$ MeV represents the pseudoscalar-meson decay constant in the chiral limit, and the inverse range parameters α_i are fitted to the low energy $\bar{K}N$ data. The indices i and j run over the meson-baryon coupled channels $\pi\Lambda$, $\pi\Sigma$, $\bar{K}N$, $\eta\Lambda$, $\eta\Sigma$, and $K\Xi$, including all their appropriate charge states. Details of the free-space version of this model are given in Ref. [20]. Here we summarize its essential points with emphasis on in-medium modifications.

The chiral symmetry of meson-baryon interactions is reflected in the structure of the C_{ij} coefficients derived directly from the Lagrangian. The exact content of the matrix elements up to second order in the meson c.m. kinetic energies was specified already in Ref. [22]. In practice, one often considers only the leading order TW interaction [5] with energy dependence given by

$$C_{ij}(\sqrt{s}) = -C_{ij}^{\text{TW}}(2\sqrt{s} - M_i - M_j)/4. \qquad (9)$$

The structure constants C_{ij}^{TW} are listed in Ref. [23]. We note that this relativistic prescription differs from the one adopted in models derived from a chiral Lagrangian formulation for static baryons [20,22] and expanded strictly only to second order in meson energies and quark masses. There, the energy dependence form $(2\sqrt{s} - M_i - M_j)$ is replaced by $(\omega_i' + \omega_j')$ where the primed meson energies ω_j' include a relativistic correction: $\omega_j' = \omega_j + (\omega_j^2 - m_j^2)/(2M_0)$, with m_j denoting the meson mass in channel j and where M_0 is the baryon mass in the chiral limit. In principle, approaches based on different formulations of the chiral Lagrangian should give identical results for physical observables. However, this is true only when one sums up an infinite series of relevant Feynman diagrams to all orders in q, and need not hold at a given perturbative order. In other words, models based on different Lagrangian formulations, or models that differ from each other in prescribing how to treat terms beyond leading order, may give within reasonable limits different predictions for physical observables.

The scattering amplitudes corresponding to the separable potentials (8) are also of a separable form

$$F_{ij}(p, p'; \sqrt{s}) = g_i(p) f_{ij}(\sqrt{s}) g_j(p'), \qquad (10)$$

with the same form factors $g_i(p)$ and $g_j(p')$, and where the *reduced* scattering amplitude f_{ij} is given explicitly by

$$f_{ij}(\sqrt{s})$$
$$= -\frac{1}{4\pi f_\pi^2} \sqrt{\frac{M_i M_j}{s}} [(1 - C(\sqrt{s}) \cdot G(\sqrt{s}))^{-1} \cdot C(\sqrt{s})]_{ij}. \qquad (11)$$

Here the meson-baryon propagator $G(\sqrt{s})$ is diagonal in the channel indices i and j. When the elementary $\bar{K}N$ system is submerged in the nuclear medium one has to consider Pauli blocking and self-energies (SE) generated by the interactions of mesons and baryons with the medium. Thus, the propagator $G(\sqrt{s})$ and the reduced amplitudes $f_{ij}(\sqrt{s})$ become dependent on the nuclear density ρ. The intermediate state Green's function is calculated as

$$G_i(\sqrt{s}; \rho)$$
$$= \frac{1}{f_\pi^2} \frac{M_i}{\sqrt{s}} \int_{\Omega_i(\rho)} \frac{d^3\vec{p}}{(2\pi)^3} \frac{g_i^2(p)}{p_i^2 - p^2 - \Pi_i(\omega_i, E_i, \vec{p}; \rho) + \mathrm{i}0}. \qquad (12)$$

Here $\vec{p}_i$ is the on-shell c.m. momentum in channel i and the integration domain $\Omega_i(\rho)$ is limited by the Pauli principle in the $\bar{K}N$ channels. Included in the denominator of the Green's function (12) is the sum Π_i of meson and baryon self-energies in channel i. In particular the kaon SE $\Pi_K = 2\omega_K V_{K^-}$, which serves as input in Eq. (12) and therefore also in Eq. (11) for the output reduced amplitude f_{K^-N}, requires by Eq. (2) the knowledge of this same output f_{K^-N}. This calls for a *self-consistent* solution of the in-medium reduced scattering amplitudes $f_{ij}(\sqrt{s}, \rho)$ as was first suggested by Lutz [24]. In the present calculation, following Ref. [15], the baryon and pion self-energies were approximated by momentum independent potentials $V = V_0 \rho/\rho_0$ with real and imaginary parts of V_0 chosen consistently from mean-field potentials used in nuclear structure calculations and in scattering calculations, respectively. Specifically, we adopted $V_0^\pi = (30 - \mathrm{i}10)$ MeV, $V_0^\Lambda = (-30 - \mathrm{i}10)$ MeV, $V_0^\Sigma = (30 - \mathrm{i}10)$ MeV, and $V_0^N = (-60 - \mathrm{i}10)$ MeV.

The free parameters of the separable-interaction chiral models considered in Ref. [20] and in the present work were fitted to the available experimental data on low energy $\bar{K}N$ interactions, consisting of K^-p low-energy cross sections for elastic scattering and reactions to the $\bar{K}^0n$, $\pi^+\Sigma^-$, $\pi^-\Sigma^+$, $\pi^0\Lambda$ and $\pi^0\Sigma^0$ channels (as listed in Ref. [22]). In addition, the accurately determined K^-p threshold branching ratios γ, R_c, R_n [25] provide a rather strict test for any quantitative model. Another stringent test is provided by the recent SIDDHARTA measured values ΔE_{1s} and Γ_{1s} of the K^-–hydrogen atom $1s$ level shift and width [21].

In the present work we focus on a separable-interaction LO chiral model marked TW1, constructed by fitting just two parameters to the data, $f_\pi = 113 \pm 2$ MeV for the PS meson decay constant and $\alpha = 701 \pm 20$ MeV for the common inverse range parameter, both within one's theoretical expectations. Some characteristics of the TW1 model in comparison to other LO models are listed in Table I. These LO models include only the leading TW interaction [5], with interchannel couplings given by Eq. (9). Also listed in the table are the positions z_1, z_2 of the two $I = 0$ S-matrix poles that reside on the second Riemann sheet $[-, +]$ of the complex energy manifold, where the signs are those of the imaginary parts of the c.m. momenta in the $\pi\Sigma$ and $\bar{K}N$ channels, respectively. Their origin may be traced to poles in decoupled $I = 0$ channels, a $\pi\Sigma$ resonance pole $z_1^{(0)}$ and a $\bar{K}N$ quasibound state pole $z_2^{(0)}$.
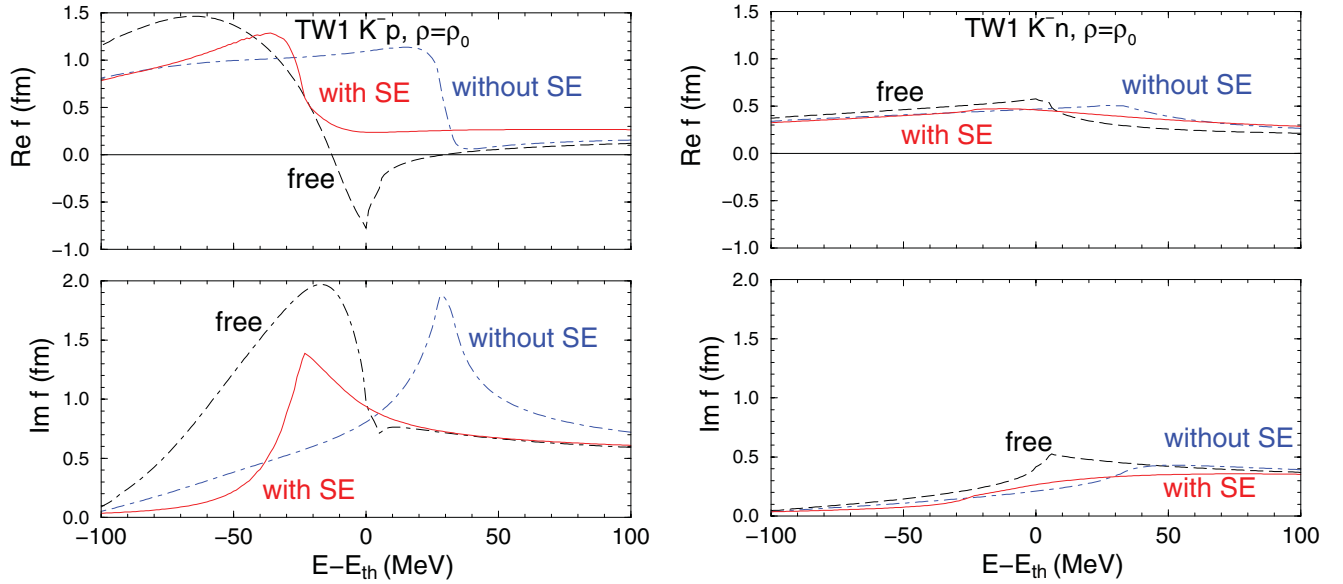
TABLE I. K^-p threshold observables calculated in several free-space LO coupled-channel chiral models. The K^-–hydrogen atom $1s$ shift ΔE_{1s} and width Γ_{1s} (in eV) marked by asterisks were obtained from the calculated K^-p scattering length by means of a modified Deser-Trueman relation [26] and are compared to the SIDDHARTA measured values [21]. The K^-p threshold branching ratios γ, R_c, R_n are from Ref. [25]. The last two columns list the calculated $I = 0$ S-matrix pole positions z_1, z_2 (in MeV) on the $[-, +]$ second Riemann sheet of the complex energy plane.

	ΔE_{1s}	Γ_{1s}	γ	R_c	R_n	z_1	z_2
TW1	323	659	2.36	0.636	0.183	(1371, −54)	(1433, −25)
JOORM [27]	275*	586*	2.30	0.618	0.257	(1389, −64)	(1427, −17)
HW [28]	270*	570*	1.80	0.624	0.225	(1400, −76)	(1428, −17)
exp.	283	541	2.36	0.664	0.189	–	–
error (±)	42	111	0.04	0.011	0.015	–	–

FIG. 1. (Color online) Energy dependence of the c.m. reduced amplitudes f_{K^-p} (left panels) and f_{K^-n} (right panels) in model TW1. The upper and lower panels refer to the real and imaginary parts of f, respectively. Dashed curves: free space, dot-dashed: Pauli blocked amplitude (without SE) at $\rho = \rho_0$, solid curves: including meson and baryon self-energies (with SE) at $\rho = \rho_0$.

The $\pi\Sigma$-$\bar{K}N$ interchannel coupling moves the poles away from their zero-coupling position, the precise full-coupling position exhibiting some model dependence. It is remarkable that all the LO TW models listed in the table are in close agreement on the position of the upper pole z_2. This agreement is spoiled when NLO corrections that require additional low energy constants to be fitted to the experimental data are included in the interchannel couplings. In contrast, the position of the lower pole z_1 exhibits model dependence already in TW models. Generally, it is located much further away from the real axis than the pole z_2. The pole z_2 is usually relegated to the subthreshold behavior of the K^-p amplitude and to the $\Lambda(1405)$ resonance observed in the $\pi\Sigma$ mass spectrum in $\bar{K}N$ initiated reactions. Nuclear medium effects on the poles z_1, z_2 are discussed in the Appendix.

In Fig. 1 we show the energy dependence of the reduced elastic scattering amplitudes f_{K^-p} and f_{K^-n} in model TW1 in free space and for two versions of in-medium modifications (marked "with" and "without" SE). Recall that $f_{K^-p} = \frac{1}{2}(f_{\bar{K}N}^{I=0} + f_{\bar{K}N}^{I=1})$ is affected by the subthreshold $I = 0$ $\Lambda(1405)$ resonance, whereas $f_{K^-n} = f_{\bar{K}N}^{I=1}$ is not affected. Indeed, the free-space amplitudes, in dashed lines, exhibit a marked difference between K^-p and K^-n, with the former amplitude showing a typical resonance structure. The pronounced peak in Im f_{K^-p} and the change of sign in Re f_{K^-p} point to the existence of a quasibound state generated by the $I = 0$ $\bar{K}N$ interaction closely below the K^-p threshold. In contrast, the pure $I = 1$ K^-n amplitude displays hardly any energy dependence besides a smooth and slow decrease of the imaginary part upon going to subthreshold energies where phase space cuts it down. The free-space K^-n interaction is weakly attractive and its in-medium renormalization, given by the other curves on the right-hand panels, is rather weak and exhibits little density dependence, in clear distinction to

the in-medium effect on the K^-p amplitudes shown on the left-hand panels. Here, in-medium Pauli blocking moves the K^-p free-space resonance structure to higher energies, as demonstrated by the dot-dashed lines (marked "without SE") in the left panels of the figure which correspond to nuclear matter density $\rho_0 = 0.17\,\text{fm}^{-3}$. The TW1 results obtained here with Pauli blocking fully agree with those obtained long ago by Waas, Kaiser, Weise [6] and which are recoverable upon switching on their parameter set in our chiral formulation. In contrast, a very different pattern was presented by Ramos and Oset [14], most likely due to their on-shell treatment of the intermediate state propagator and the inclusion of a "nucleon hole" term.

The effect of combined Pauli blocking and hadron SE on the K^-p amplitude is shown by the solid lines (marked "with SE") in Fig. 1. The real part of the amplitude remains positive (attractive) in the whole energy range, in agreement with phenomenological analyses of kaonic atoms [7], while the peak of the imaginary part moves back to approximately where it was in the free-space amplitude. The most striking feature of the model is the sharp increase in the real part of the amplitude when going to subthreshold energies, caused mainly by the introduction of kaon self energy in the propagator (12) which is responsible for moving the resonant structure related to the $\Lambda(1405)$ back below the $\bar{K}N$ threshold. Consequently, the K^-p interaction becomes much stronger at energies about 30 MeV below the K^-p threshold with respect to its strength at threshold. This feature is missing in the in-medium calculations of Ref. [14] which get substantially different results than ours already when only Pauli blocking is accounted for.

Although the simple LO TW1 model was used to demonstrate the nuclear medium effect on the K^-p interaction in Fig. 1, the same pattern is obtained within the NLO CS30
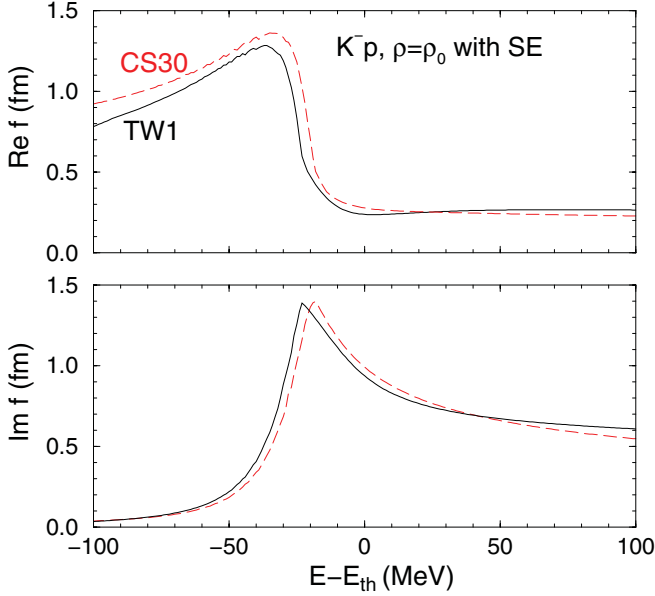
FIG. 2. (Color online) Energy dependence of the in-medium c.m. reduced amplitude f_{K^-p} at nuclear matter density ρ_0 in models TW1 (solid lines) and CS30 (dashed lines). The calculations include Pauli blocking and self-energies.

FIG. 3. (Color online) Energy dependence of the c.m. reduced amplitude f_{K^-N} (13) in model TW1 below and above threshold. Dashed curves: in free-space; dot-dashed curves: Pauli blocked amplitude at $0.5\rho_0$; solid curves: including meson and baryon self-energies at $0.5\rho_0$.

model of Ref. [20]. This is demonstrated in Fig. 2 where in-medium "with SE" K^-p reduced scattering amplitudes generated in these two models are compared to each other at $\rho = \rho_0$. The differences between the two sets of curves are seen to be minute.

To end this section we show in Fig. 3, for model TW1, the reduced scattering amplitude corresponding to the interaction of K^- mesons with symmetric nuclear matter,

$$f_{K^-N}(\sqrt{s}, \rho) = \tfrac{1}{2}[\, f_{K^-p}(\sqrt{s}, \rho) + f_{K^-n}(\sqrt{s}, \rho)\,], \qquad (13)$$

where $f_{K^-N}(\sqrt{s}, \rho = 0) \equiv f_{K^-N}(\sqrt{s})$. The free-space amplitude $f_{K^-N}(\sqrt{s})$, for $\rho = 0$, is marked by dashed lines. Its imaginary part peaks about 15 MeV below the $\bar{K}N$ threshold, and its real part rapidly varies there from weak attraction above to strong attraction below threshold. While $f_{K^-N}(\sqrt{s})$ at and near threshold is constrained by data that serve to determine the parameters of the chiral model, the extrapolation to the subthreshold region may suffer from ambiguities depending on the applied model [2]. Also shown in Fig. 3 are two versions of in-medium reduced amplitudes $f_{K^-N}(\sqrt{s}, \rho = 0.5\rho_0)$. One version, in dot-dashed lines (marked "without SE"), implements Pauli blocking in the intermediate $\bar{K}N$ states for $\rho \neq 0$. The resulting f_{K^-N} exhibits a resonance-like behavior about 20 MeV above threshold, in agreement with Ref. [6]. The other in-medium version, in solid lines (marked "with SE"), adds self-consistently meson and baryon self-energies in intermediate states, as explained earlier. The resulting in-medium f_{K^-N} is strongly energy dependent, with a resonance-like behavior about 35 MeV below threshold. Similar results are obtained at full nuclear matter density $\rho_0 = 0.17$ fm^{-3}. We note that whereas the two in-medium reduced amplitudes shown in the figure are close to each other far below and far above threshold, they differ substantially at
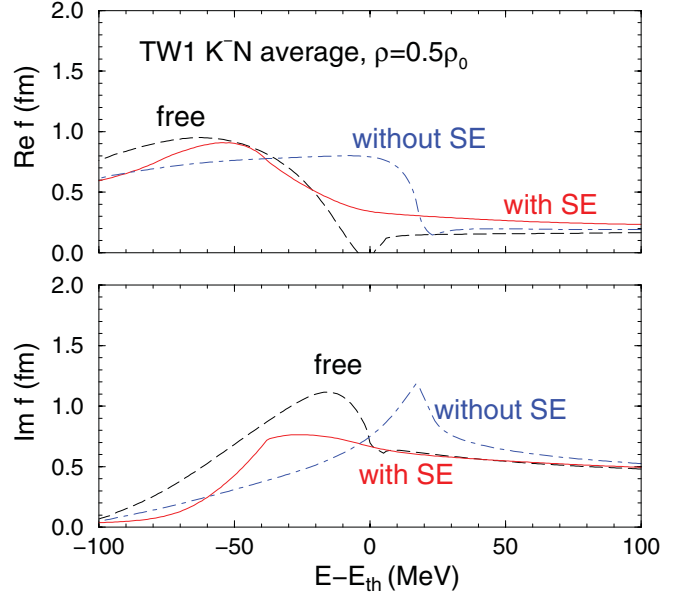
and near threshold. This applies also to the full amplitudes F_{K^-N}, Eq. (10), since the form factors $g(p)$ remain the same in the transition from free-space to in-medium separable amplitudes. At threshold, in particular, the real part of the "with SE" amplitude is about half of that "without SE," corresponding to a depth $-\mathrm{Re}\, V_{K^-}(\rho_0) \approx 40$ MeV, in rough agreement with Ref. [14].

IV. K^- ATOM CALCULATIONS

Strong interaction level shifts and widths in kaonic atoms have been for decades a source of precise data on the K^- nuclear interaction near threshold. Particularly instructive are so-called "global" analyses when data for many nuclei across the periodic table are being analyzed together, usually with the help of optical potentials which are related to the nuclear densities [10]. This type of analyses could reveal characteristic features of the interaction which, in turn, reflect on the underlying K^-N interaction in the medium, for example, its energy and density dependence. It was shown already in 1993 [7] that with density-dependent empirical amplitudes within a "$t\rho$" approach to the optical potential, very good fits to the data were possible. Depths of the real potential were close to 180 MeV whereas fixed-t models achieved inferior fits and the resulting potentials were half as deep. Later predictions of in-medium chiral models *at threshold* [14] presented depths of only 50 MeV for the real potential at full nuclear density. This wide span of values has been termed the "deep vs shallow" controversy in kaonic atoms [29]. While attention has been focused on depths of the potentials, little attention was paid to the other empirical finding [7], namely, that the best-fit real potentials were not only deep but also *"compressed"* relative

to the corresponding nuclear densities, with rms radii smaller than the nuclear rms radii. This feature means that the real part of the underlying K^--bound nucleon interaction increases with density, and it is shown below to be in line with the density dependence of the chiral model in-medium amplitudes employed in the present work.

A. Wave equation

The choice of K^- wave equation follows naturally from the in-medium dispersion relation

$$\omega_K^2 - \vec{p}_K^2 - m_K^2 - \Pi_K(\vec{p}_K, \omega_K, \rho) = 0, \qquad (14)$$

where $\Pi_K(\vec{p}_K, \omega_K, \rho) = 2(\mathrm{Re}\,\omega_K)V_{K^-}$ is the self-energy (SE) operator for a K^- meson with momentum $\vec{p}_K$ and energy ω_K [30]. The Klein-Gordon (KG) dispersion relation (14) leads in hadronic atoms applications to a KG equation satisfied by the K^- wave function [10]:

$$\left[\nabla^2 - 2\mu(\mathcal{B}_K + V_c) + (V_c + \mathcal{B}_K)^2 + 4\pi \left(1 + \frac{A-1}{A}\frac{\mu}{m_N}\right) \right.$$
$$\left. \times F_{K^-N}(\vec{p}, \sqrt{s}; \rho)\, \rho \right] \psi = 0. \qquad (15)$$

Here, μ is the K^--nucleus reduced mass, $\mathcal{B}_K = B_K + i\Gamma_K/2$ is a complex binding energy, including a strong interaction width Γ_K, and V_c is the K^- Coulomb potential generated by the finite-size nuclear charge distribution, including vacuum-polarization terms.

B. s waves

The first application of the scheme presented in Sec. II for handling K^-N amplitudes below threshold was to global analyses of strong-interaction effects in kaonic atoms. The database was the same as in Ref. [7] with 65 data points for targets from ^{7}Li to ^{238}U. In solving the KG equation (15), the $\vec{p}_K$ momentum dependence of F_{K^-N} was transformed into density and energy dependence according to Eq. (6). Furthermore, proton and neutron densities were handled separately, replacing $F_{K^-N}(\sqrt{s}, \rho)\rho(r)$ by an effective amplitude

$$\mathcal{F}_{K^-N}^{\mathrm{eff}}(\sqrt{s}, \rho)\rho(r)$$
$$= F_{K^-p}(\sqrt{s}, \rho)\rho_p(r) + F_{K^-n}(\sqrt{s}, \rho)\rho_n(r), \quad (16)$$

with ρ_p and ρ_n normalized to Z and N, respectively, and $Z + N = A$. Two-parameter Fermi distributions (2pF) were used for both densities, with ρ_p obtained from the known charge distribution by unfolding the finite size of the charge of the proton. For ρ_n averages of the "skin" and "halo" forms of Ref. [31] were chosen with the difference between rms radii given by $r_n - r_p = (N - Z)/A - 0.035$ fm. The reduced amplitudes f_{K^-p} and f_{K^-n} were evaluated at $\sqrt{s}$ given by Eq. (7), where the atomic binding energy B_K was neglected with respect to $B_N \approx 8.5$ MeV. A similar approximation was made in Eq. (6) for p^2 when using the form factors $g(p)$ of Eq. (10). The K^--nucleus potentials were calculated by requiring self-consistency in solving Eq. (7) with respect to $\mathrm{Re}\,V_{K^-}$, i.e., the value of $\mathrm{Re}\,V_{K^-}(\rho)$ in the expression for
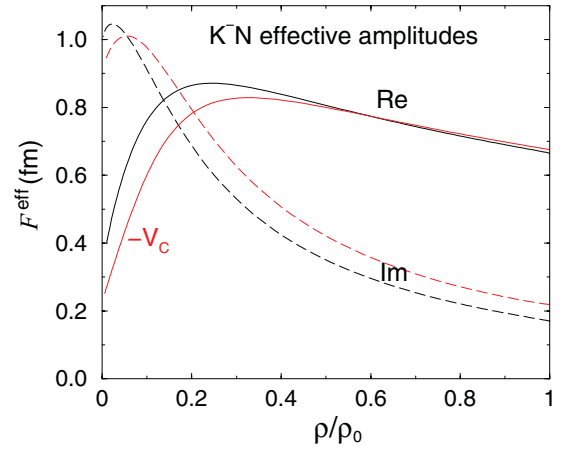

FIG. 4. (Color online) Density dependence of the in-medium "without SE" CS30 self-consistent subthreshold amplitude $\mathcal{F}_{K^-N}^{\mathrm{eff}}$ for Ni.

$\sqrt{s}$ and in the form factors g had to agree with the resulting $\mathrm{Re}\,V_{K^-}(\rho)$. That was done at each radial point and for every target nucleus in the database.

It is instructive to start by inspecting the effective amplitudes Eq. (16) obtained in the above self-consistent procedure. Figure 4 shows effective amplitudes for K^- on Ni, calculated from the CS30 "without SE" K^-N amplitudes, with and without the $\sqrt{s} \to \sqrt{s} - V_c$ substitution discussed in Sec. II. The increase of $\mathrm{Re}\,\mathcal{F}_{K^-N}^{\mathrm{eff}}(\rho)$ with density over the nuclear surface region combined with the decrease of $\mathrm{Im}\,\mathcal{F}_{K^-N}^{\mathrm{eff}}(\rho)$ are the underlying mechanisms behind the compression of the real part and inflation of the imaginary part of best-fit density-dependent phenomenological potentials [7]. Similar results for CS30 amplitudes that include SE were shown in Ref. [16]. Although there are differences in details between the various models, the geometrical implications are robust. The decrease of $\mathrm{Im}\,\mathcal{F}_{K^-N}^{\mathrm{eff}}$ with increasing density is unreasonably rapid, originating from the one-nucleon nature of the CS30 amplitudes, where, as seen in Fig. 3 for the similar TW1 amplitude, the imaginary part practically vanishes around 80 MeV below threshold. We note that multinucleon absorption processes which become increasingly important at subthreshold energies are not included in the present approach. Since strong-interaction effects in kaonic atoms are dominated by the widths, the deficiency in the imaginary part of the amplitudes must be reflected when comparing predictions with experiment. This is indeed the case with χ^2 per point of about 10.

Figure 5 shows, as representative examples, several K^-–Ni potentials based on the CS30 "without SE" amplitudes, within the self consistent procedure described above. As a reference, the curves marked DD represent the best fit purely phenomenological density-dependent potentials [7] with $\chi^2 = 103$ for 65 data points. The potential marked CS30 is without any adjustable parameters and it differs substantially from the DD reference potential. Nevertheless its real part of -85 MeV is twice as deep as the shallow potential (not shown here) of Ref. [32] which results from *threshold* values $f_{K^-N}(E_{\mathrm{th}}, \rho)$, without going subthreshold. Figure 5 also demonstrates the effect of adding adjustable ρ and ρ^2 terms to the
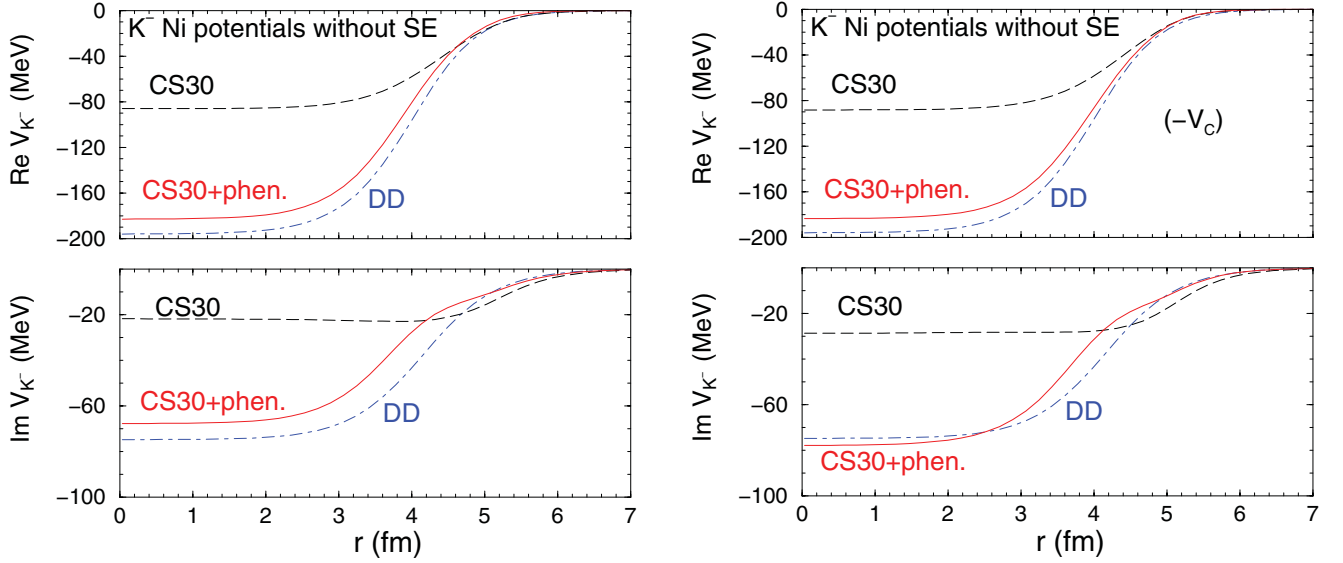
FIG. 5. (Color online) Left: K^--nuclear potentials for K^- atoms of Ni. Dashed curves: derived self consistently from in-medium CS30 amplitudes; solid curves: plus phenomenological terms from global fits; dot-dashed curves: purely phenomenological DD potentials from global fits. Right: the same as on the left, but with the substitution $\sqrt{s} \rightarrow \sqrt{s} - V_c$ in $\mathcal{F}_{K^-N}^{\text{eff}}(\sqrt{s}, \rho)$.

CS30-based potentials, resulting in best-fit potentials marked "CS30 + phen." with χ^2 of around 130–140 for 65 points, very close to χ^2 values achieved with a fixed-t approach. It is seen that the resulting "CS30 + phen." potentials are close to the DD ones and we note that the additional terms, both real and imaginary, are dominated by ρ^2 terms which are required by the fit procedure and which are likely to represent $\bar{K}NN$ absorptive and dispersive contributions, respectively. Similar results hold for in-medium TW1 amplitudes, such as shown in Fig. 3. The resulting TW1 K^- nuclear potentials are shown in Fig. 6, exhibiting remarkable similarity to the CS30 K^- nuclear potentials of Fig. 5. We note that the addition of phenomenological terms lowers the resulting χ^2 to as low a value as 124 for 65 data points.

On first sight the additional "phen." terms appear large in comparison with the one-nucleon based CS30 and TW1 potentials, particularly if one considers values of the potentials near the nuclear center. However, strong interaction effects in kaonic atoms are sensitive mostly to potential values near the nuclear surface [29], about 3.5 to 5 fm in the examples shown. It is seen from the figures that over this range of radii the phenomenological part of the imaginary potential is of the order of 30% of the starting values, consistent with the fraction of multinucleon absorptions estimated from experiments in emulsion and bubble chambers [33]. By the same token one may safely conclude that the data imply real potentials of depths 80–90 MeV near the half-density radius. Finally a significant observation is that when the CS30 or the TW1 amplitudes are taken *at threshold*, then the additional phenomenological potential is no longer dominated by ρ^2 terms. In particular, *negative* imaginary ρ^2 terms are obtained, thus defying a two-nucleon absorption interpretation. The emerging phenomenology is similar to that for V_{π^-} in pionic atom studies where theoretically motivated single-nucleon contributions are augmented by phenomenological ρ^2 terms

representing πNN processes [34]. More work is required to justify microscopically the size of the ρ^2 kaonic atom contributions suggested by successful $V_{K^-}^{\text{chiral+phen.}}$ potentials.

C. Adding p waves

Next we turn to the question of whether kaonic atom data support contributions from a p-wave term in the K^-N
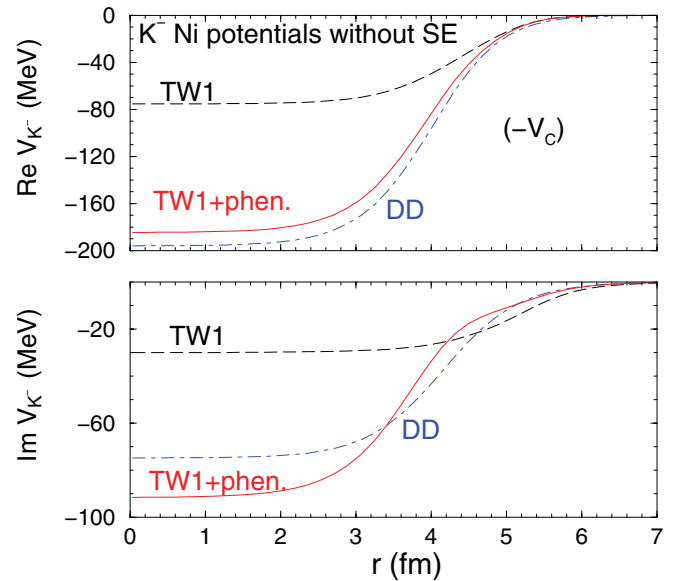

FIG. 6. (Color online) K^- nuclear potentials for K^- atoms of Ni. Dashed curves: derived self-consistently from in-medium TW1 amplitudes; solid curves: plus phenomenological terms from global fits; dot-dashed curves: purely phenomenological DD potentials from global fits.

TABLE II. Results of $t\rho$ global fits to kaonic atoms data.

χ^2 ($N = 65$)	Re b_0 (fm)	Im b_0 (fm)	Re c_0 (fm^3)	Im c_0 (fm^3)
132	0.60 ± 0.05	0.94 ± 0.05	–	–
110	0.73 ± 0.09	0.59 ± 0.09	-0.79 ± 0.32	0.75 ± 0.30

interaction and, for reference, we first checked the effect of including such a phenomenological term in a $t\rho$ potential. A p-wave term was added to the simplest $t\rho$ s-wave potential as follows [10]:

$$2\mu V_{K^- N}(r) = q(r) + \vec{\nabla} \cdot \alpha(r)\vec{\nabla} \qquad (17)$$

with $q(r)$ its s-wave part given by

$$q(r) = -4\pi \left(1 + \frac{\mu}{m_N}\right) b_0[\rho_n(r) + \rho_p(r)] \qquad (18)$$

and the p-wave part given by

$$\alpha(r) = 4\pi \left(1 + \frac{\mu}{m_N}\right)^{-1} c_0[\rho_n(r) + \rho_p(r)]. \qquad (19)$$

Terms proportional to $\rho_n(r) - \rho_p(r)$ are neglected here.

It is seen from Table II that an improved fit to the data is obtained with some of the absorption shifted from the s-wave term into the p-wave term which is repulsive and, thereby, the s-wave attraction required to fit the data is enhanced. However, this could also be just a numerical effect of the χ^2 fit process "compressing" the real part of the otherwise s-wave $t\rho$ potential, as noted above.

The empirical p-wave term may be compared, for example, with the $K^- p$ p-wave amplitude of Weise and Härtle [30] which is dominated by the $I = 1$ $\Sigma(1385)$ subthreshold resonance. Over the energy range between about 1385 MeV and the $K^- N$ threshold at 1432 MeV the $K^- p$ p-wave amplitude is approximated there by

$$c_{K^- p} = \frac{\sqrt{s}\gamma_1}{s_0 - s - i\sqrt{s}\Gamma(\sqrt{s})} + d \qquad (20)$$

with $\sqrt{s_0} = 1385$ MeV, $\gamma_1 = 0.42/m_K^3$, $\Gamma(\sqrt{s}) \approx 40$ MeV and a background term $d = 0.06$ fm^3. Considering that $c_{K^- n} = 2c_{K^- p}$ for an $I = 1$ dominated amplitude, then for $\rho_p \approx \rho_n$ and neglecting $\rho_n - \rho_p$ terms in the empirical potential, $c_{K^- p}$ is to be multiplied by 3/2 in order to compare with the above c_0. Table III shows calculated values for a "microscopic" $c_0^m = (3/2)c_{K^- p}$ obtained for $\sqrt{s}$ given by Eq. (7), here applied to Ni.

It is seen that at threshold the empirical c_0 is an order of magnitude too large compared to its "microscopic" counterpart c_0^m. Averaging over subthreshold energies is unlikely to produce agreement between the two.

The natural next step was to include $c_{K^- p}$ of Eq. (20) in the subthreshold evaluation of the s-wave potential to create also a $K^- N$-based p-wave potential. This was done at each radial point for the local density and the $\sqrt{s}$ obtained self-consistently for the dominant s-wave potential. Without any adjustable parameters it reduced the CS30-based χ^2 from ≈ 10 per point to about 6 per point. Including also two scaling factors, for the resonance part and for the background part

of Eq. (20) and searching on these parameters, yielded a scaling factor -0.025 ± 0.029 for the resonance and 3.5 ± 0.1 for the background, with $\chi^2 \approx 3$ per point. It means that within the subthreshold approach to the $K^- N$ interaction a resonance term in the p-wave interaction is not required to fit the data. This is consistent with the first comprehensive phenomenological analysis of $\bar{K}N$–πY coupled channels by Kim [35], concluding that the $\Sigma(1385)$ is definitely not a p-wave $\bar{K}N$ bound state, but rather a $\pi\Lambda$ scattering resonance with very weak coupling to the $\bar{K}N$ channel. This conclusion was reinforced in a dispersion relation analysis by Martin [25] in which the $\bar{K}N$ channel coupled very weakly, compatible with zero coupling to the $\Sigma(1385)$ resonance. Finally, the p-wave amplitude $c_{K^- p}$ of Eq. (20) was included in the "CS30 + phen." fits, where ρ and ρ^2 terms were added to the CS30 potentials. Again the resonance term was found to vanish and only a small p-wave constant background term was acceptable. It is therefore concluded that fits to kaonic atom data do not require a resonant p-wave term within the subthreshold self-consistent approach of the present work.

V. CALCULATIONS OF K^- NUCLEAR QUASIBOUND STATES

Quasibound K^- nuclear states in several nuclei across the periodic table were calculated in Refs. [3,9] within the relativistic mean field (RMF) model for nucleons and antikaons. The energy independent K^- nuclear real potential $V_{K^-}^{\mathrm{RMF}}$ was supplemented in these calculations by a phenomenological "$t\rho$" imaginary potential Im V_{K^-} with energy dependence that accounted for the reduced phase-space available for in-medium K^- absorption. Two-nucleon absorption terms were also included.

The present formulation differs fundamentally from these previous RMF calculations in that we use a K^- nuclear potential V_{K^-} given by Eq. (2) in terms of energy and density dependent in-medium $K^- N$ scattering amplitudes $F_{K^- N}(\vec{p}, \sqrt{s}, \rho)$

TABLE III. Values of a "microscopic" p-wave amplitude $c_0^m = (3/2)c_{K^- p}$ [see Eq. (20)] to be compared with the empirical c_0 of Table II.

ρ/ρ_0	$\sqrt{s}$ (MeV)	Re c_0^m (fm^3)	Im c_0^m (fm^3)
0	1432	-0.09	0.08
0.25	1420	-0.12	0.12
0.50	1404	-0.16	0.25
0.75	1392	-0.06	0.44
1.00	1382	0.10	0.49

generated from a well-defined coupled-channel chiral model. The momentum dependence of F_{K^-N} was transformed into energy and density dependence using Eq. (6). The in-medium KG dispersion relation (14) leads to a bound-state KG equation satisfied by the K^- wave function which is written here in the form

$$\left[\nabla^2 + \omega_K^2 - m_K^2 + 4\pi \frac{\sqrt{s}}{m_N} F_{K^-N}(\sqrt{s}, \rho)\rho\right]\psi = 0, \quad (21)$$

where

$$\omega_K = m_K - \mathcal{B}_K - V_c , \quad (22)$$

$\mathcal{B}_K = B_K + i\Gamma_K/2$ and $\sqrt{s}$ is given by Eq. (7) which now also includes the substitution $\sqrt{s} \to \sqrt{s} - V_c$:

$$\sqrt{s} \approx E_{\text{th}} - B_N - \xi_N(B_K + V_c) - 15.1\left(\frac{\rho}{\rho_0}\right)^{2/3}$$
$$+ \xi_K \text{Re } V_{K^-}(\rho). \quad (23)$$

Equation (21) differs from the K^- atom equation (15) by A^{-1} correction terms. Since B_K and $V_{K^-}(\rho)$ appear through Eq. (23) in the argument $\sqrt{s}$ of F_{K^-N} (the latter is essentially V_{K^-}), it suggests a self-consistency scheme in terms of *both* B_K and $V_{K^-}(\rho)$ for solving the KG equation (21). In order to study the effect of energy and density dependencies of the argument $\sqrt{s}$ of the chiral K^-N scattering amplitude F_{K^-N}, we first solved the KG equation in a static approximation, switching off the RMF self-consistency cycle that accounts for the modification of the nuclear density by the strongly bound K^- meson and its effect on the binding energy B_K. Self-consistency with respect to B_K and $V_{K^-}(\rho)$, however, remained operative in the static approximation. Realistic RMF density distributions $\rho(r)$ of the core nuclei were employed.

In Table IV, we list binding energies B_K and widths Γ_K of $1s$ K^- nuclear quasibound states obtained by solving Eq. (21) self-consistently in several nuclei across the periodic table, using in-medium "no SE" and "+SE" TW1 subthreshold amplitudes with argument $\sqrt{s}$ given by Eq. (23) (denoted "$\sqrt{s}$" in the table). These values of B_K and Γ_K are compared to those calculated using threshold amplitudes without undergoing self consistency cycles (denoted "E_{th}" in the table). The table illustrates the peculiar role of energy dependence of the $\bar{K}N$ scattering amplitudes. In the "no SE" case, when the in-medium effects consist only of Pauli blocking, the self-consistent calculations with subthreshold amplitudes yield lower B_K values compared to those calculated using threshold amplitudes. In contrast, in the "+SE" case, when hadron in-medium self-energies are included, the self-consistent calculations with subthreshold amplitudes yield considerably higher B_K values compared to those calculated using threshold amplitudes (in which case the $1s$ state in ^{12}C is even unbound). It is worth noting that the self-consistent calculations of B_K give very similar results in the "+SE" version to those in the "no SE" version, as could be anticipated from the deep-subthreshold portion of the scattering amplitudes shown in Fig. 1. These B_K values are also remarkably close to those calculated within a static RMF approach for nucleons and antikaons, when the K^- nucleus

TABLE IV. Binding energies B_K and widths Γ_K (in MeV) of $1s$ K^- nuclear quasibound states in several nuclei, calculated using static RMF nuclear densities in Eq. (21) and TW1 chiral amplitudes with (i) $\sqrt{s} = E_{\text{th}}$ and (ii) $\sqrt{s}$ from Eq. (23), in both in-medium versions "no SE" and "+SE." $K^-NN \to YN$ decay modes are excluded. Results of static RMF calculations of B_K, with a K^- nuclear interaction mediated by vector mesons only, are shown for comparison in the last row.

		^{12}C	^{16}O	^{40}Ca	^{90}Zr	^{208}Pb
E_{th}, no SE	B_K	61.1	57.5	83.4	96.0	104.8
	Γ_K	149.1	135.9	150.7	151.2	143.9
$\sqrt{s}$, no SE	B_K	40.9	42.4	58.5	69.5	77.6
	Γ_K	29.4	30.8	23.6	22.4	22.0
E_{th}, +SE	B_K	(−0.9)	6.4	25.0	39.0	53.4
	Γ_K	(137.6)	120.2	141.8	141.0	129.1
$\sqrt{s}$, +SE	B_K	42.4	44.9	58.8	68.9	76.3
	Γ_K	16.5	16.2	12.0	11.5	11.3
$V_{K^-}^{\text{RMF}}$	B_K	49.1	47.7	60.5	69.6	76.8

interaction is mediated exclusively by vector mesons with purely vector SU(3) F-type couplings, as shown in the last row of Table IV.

The calculated widths displayed in Table IV represent only $K^-N \to \pi Y$ decays, accounted for by the coupled-channel chiral model. The widths are very large in both "no SE" and "+SE" in-medium versions when using threshold amplitudes, and are considerably smaller in the self-consistent calculations using subthreshold amplitudes owing to the proximity of the $\pi\Sigma$ thresholds. In this case the "+SE" widths are about half of the "no SE" widths and approximately 10% of those calculated using threshold amplitudes.

The sensitivity of the calculated K^- binding energies and widths to the specific form of the in-medium subthreshold extrapolation of $\sqrt{s}$ is demonstrated in Fig. 7. Here, $1s$ states in several nuclei are calculated self-consistently in the "no SE" version within the TW1 model for $\sqrt{s} = E_{\text{th}} - B_K$ (dotted line), $\sqrt{s} = E_{\text{th}} - B_K - V_c$ (dashed line), $\sqrt{s}$ of Eq. (23) (dot-dashed line), and for the latter $\sqrt{s}$ choice also in the "SE" version (full line). To lead the eye, each of the four lines connects (B_K, Γ_K) values in different core nuclei using one of the above forms for $\sqrt{s}$. It is seen that the specific form chosen to extrapolate $\sqrt{s}$ has a relatively small effect on the binding energies B_K, which vary within 5 MeV for a particular nucleus. In contrast, the widths are reduced significantly from about 55 ± 10 MeV to 14 ± 3 MeV, when $\sqrt{s}$ is shifted further below threshold and the "SE" version which incorporates in-medium hadron self-energies is applied.

Figure 8 illustrates the model dependence of K^- nuclear quasibound state calculations by showing binding energies and widths of $1s$ states in several nuclei calculated self-consistently by applying the subthreshold extrapolation $\sqrt{s} = E_{\text{th}} - B_K - V_c$ [30] to the TW1 and CS30 in-medium "no SE" amplitudes. It is seen that the K^- binding energies are more sensitive to the applied chiral model than to the form of subthreshold $\sqrt{s}$ extrapolation exhibited in Fig. 7. However, the difference in widths for a given nucleus is comparable to the differences due to the various forms of subthreshold $\sqrt{s}$ extrapolation shown
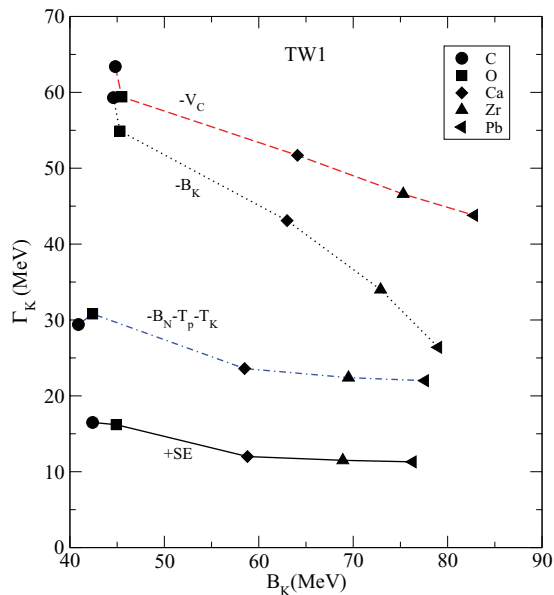
FIG. 7. (Color online) Binding energies B_K and widths Γ_K (in MeV) of $1s$ K^- nuclear quasibound states, calculated by applying self-consistently several prescriptions of subthreshold $\sqrt{s}$ extrapolation with static RMF nuclear densities to in-medium TW1 amplitudes ("no SE" unless specified "+SE"). $K^-NN \to YN$ decay modes are excluded.

FIG. 8. (Color online) Binding energies B_K and widths Γ_K (in MeV) of $1s$ K^- nuclear quasibound states, calculated by applying self-consistently the subthreshold extrapolation $\sqrt{s} = E_{th} - B_K - V_c$ [30] with static RMF nuclear densities to the TW1 and CS30 in-medium "no SE" amplitudes. $K^-NN \to YN$ decay modes are excluded.

there. The CS30 model produces higher binding energies and lower values of widths than in the TW1 model, with a difference of approximately 10 MeV. This systematics is explained by the stronger downward energy shift induced in CS30 with respect to TW1.

Effects of including a p-wave $\bar{K}N$ interaction assigned to the $\Sigma(1385)$ subthreshold resonance are demonstrated in Table V within the "no SE" in-medium version of TW1 chiral amplitudes, for two subthreshold $\sqrt{s}$ extrapolations: [WH] denotes the form $\sqrt{s} = E_{th} - B_K - V_c$ which was applied by Weise and Härtle [30] self-consistently to chiral $\bar{K}N$ amplitudes within a local density approximation to calculate K^- nuclear $1s$ quasibound states in ^{16}O and ^{208}Pb; and $\sqrt{s}$ corresponds to the energy argument of Eq. (23). For the p-wave amplitude we adopted the parametrization (20) from Ref. [30], used also in the previous section on kaonic atoms. The calculated binding energies and widths result from a delicate interplay between the energy dependent s-wave and p-wave amplitudes. The effect of p waves is more pronounced in light nuclei where surface contributions are relatively more important, and it decreases with increasing size of the nucleus. The p-wave interaction leads to larger (smaller) widths in the [WH] ($\sqrt{s}$) version and increases the K^- binding energies, with the exception of ^{12}C and ^{16}O in the [WH] subthreshold extrapolation where the substantially increased absorption acts repulsively to reduce B_K.

Table VI presents binding energies and widths of $1s$ K^- nuclear quasibound states in several nuclei across the periodic table, calculated self-consistently within in-medium versions of CS30 chiral amplitudes. The first two sequences denoted [WH] and $\sqrt{s}$ illustrate the role of subthreshold
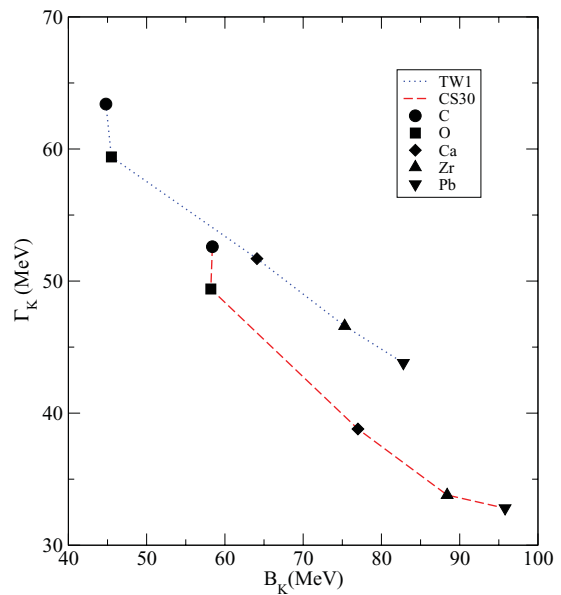
$\sqrt{s}$ extrapolation which affects particularly the widths Γ_K, in a similar pattern to that already shown for the TW1 model in Table V. The next three sequences exhibit the effects of successively sophisticating the calculations: first, the in-medium "no SE" amplitudes are dressed by self-energies (denoted "+SE"), bringing the calculated widths further down (and marginally so the binding energies); then, the calculations are made dynamical (denoted "+dyn.") taking into account the polarization of the nuclear core by the strongly bound K^-, which produces higher binding energies B_K and smaller widths Γ_K; and last, energy dependent imaginary ρ^2 terms are added self-consistently to simulate two-nucleon $K^-NN \to YN$ absorption modes (denoted "+2N abs.") and their available phase space [3,9]. Whereas the binding energies

TABLE V. Binding energies B_K and widths Γ_K (in MeV) of $1s$ K^- nuclear quasibound states in several nuclei, calculated self-consistently using static RMF nuclear densities and the in-medium "no SE" version of TW1 chiral amplitudes with (i) $\sqrt{s} = E_{th} - B_K - V_c$ and (ii) $\sqrt{s}$ from Eq. (23), without and with p-wave amplitudes. $K^-NN \to YN$ decay modes are excluded.

		^{12}C	^{16}O	^{40}Ca	^{90}Zr	^{208}Pb
WH	B_K	44.8	45.5	64.1	75.3	82.8
	Γ_K	63.4	59.4	51.7	46.6	43.8
[WH], $+p$ wave	B_K	39.7	43.7	69.1	79.9	87.2
	Γ_K	85.6	73.6	55.5	46.7	44.3
$\sqrt{s}$	B_K	40.9	42.4	58.5	69.5	77.6
	Γ_K	29.4	30.8	23.6	22.4	22.0
$\sqrt{s}$, $+p$ wave	B_K	46.0	46.0	60.8	71.5	79.4
	Γ_K	27.5	29.6	22.4	21.3	21.0

TABLE VI. Binding energies B_K and widths Γ_K (in MeV) of $1s$ K^- nuclear quasibound states in several nuclei, calculated self-consistently using in-medium CS30 chiral amplitudes in the 'no SE' version (first two sequences) and in the "+SE" version (last three sequences) for various subthreshold $\sqrt{s}$ extrapolations marked as in Table V. A combined nucleons+antikaon RMF scheme is applied dynamically in the last two sequences, and $K^-NN \to YN$ decay modes are included in the last sequence ("+2N abs.").

		^{12}C	^{16}O	^{40}Ca	^{90}Zr	^{208}Pb
WH	B_K	58.4	58.2	77.0	86.7	95.8
	Γ_K	52.6	49.8	33.8	33.8	32.8
$\sqrt{s}$	B_K	52.0	53.0	69.7	81.5	89.6
	Γ_K	19.6	21.6	14.4	13.6	14.0
+SE	B_K	50.7	52.5	68.2	79.3	86.6
	Γ_K	13.0	12.8	10.9	11.0	10.9
+dyn.	B_K	55.7	56.0	70.2	80.5	87.0
	Γ_K	12.3	12.1	10.8	10.9	10.8
+2N abs.	B_K	54.0	55.1	67.6	79.6	86.3
	Γ_K	44.9	53.3	65.3	48.7	47.3

decrease insignificantly, the resulting widths of order $\Gamma_K \sim 50$ MeV become comparable in light nuclei to the binding energies B_K.

VI. CONCLUSION

In this work we have used several versions of in-medium $\bar{K}N$ scattering amplitudes constructed in a chirally motivated coupled channel separable potential model to derive self-consistently the K^- nuclear potential for several bound state applications. The $\bar{K}N$ scattering amplitudes exhibit, invariably, a strong energy and density dependence below threshold, which reflects the dominant effect of the $\Lambda(1405)$ subthreshold resonance. This is precisely the energy region relevant for the self consistent construction of V_{K^-} for kaonic atoms and for K^- nuclear quasibound state calculations. It was found that kaonic atoms probe $\bar{K}N$ c.m. energies typically 30–50 MeV below threshold whereas K^- nuclear $1s$ quasibound states reach considerably lower $\bar{K}N$ subthreshold energies. Thus, the chiral model versions used in the present work produced potential depths in the range $-\text{Re}\,V_{K^-}^{\text{chiral}}(\rho_0) \sim 80$–90 MeV in kaonic atoms, and somewhat deeper potentials of depths 100–110 MeV for K^- nuclear quasibound states. By comparing the size and shape of our subthreshold $\bar{K}N$ scattering amplitudes with those of other chiral models, as discussed for example in Ref. [28], we expect these results to hold generally in any coupled-channel chiral model constrained by low energy K^-p data once our self-consistency construction is applied. The density dependence of the resulting kaonic atom potentials is such that by adding adjustable phenomenological terms to be determined by fits to the data, the real part of the potential becomes twice as deep and the imaginary part about three times as deep due to a ρ^2-dominated complex term which could represent $\bar{K}NN \to YN$ dispersive and absorptive modifications. These substantial modifications at full nuclear density represent extrapolations from the nuclear
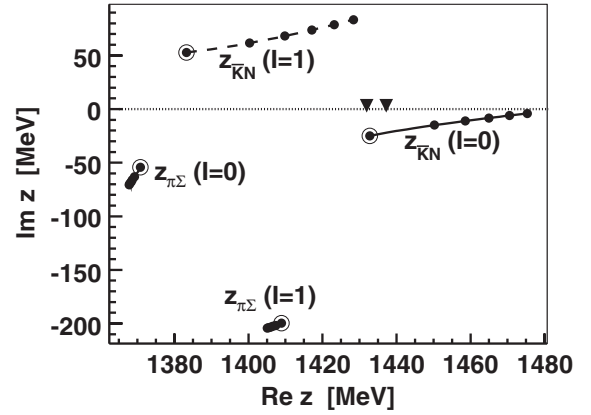

FIG. 9. Pole movements on the complex energy manifold due to the increased effect of Pauli blocking in model TW1. $I = 0$ pole trajectories are marked by full lines, $I = 1$ pole trajectories by dashed lines. Pole positions in free space are encircled and the bullets mark pole positions for $\rho = x\rho_0$ for increments of x between 0 to 1, see text for more details. The solid triangles denote the K^-p and $\bar{K}^0n$ thresholds.

surface region to which kaonic atoms are mostly sensitive and where such modifications appear more modest. More work is needed to explain the origin and test the existence of the sizable ρ^2 term. Finally, the effects of a p-wave interaction generated by the $\Sigma(1385)$ subthreshold resonance are found secondary to the effects of the s-wave interaction which is dominated by the $\Lambda(1405)$ subthreshold resonance.

APPENDIX: IN-MEDIUM POLE TRAJECTORIES

The observed properties of in-medium $\bar{K}N$ interaction may be related to the dynamics of the $\Lambda(1405)$ resonance in the nuclear medium. This is demonstrated for model TW1 in Fig. 9 which shows the motion in the complex energy plane of poles related to the $\pi\Sigma$ and $\bar{K}N$ channels upon increasing the nuclear density, including Pauli blocking but disregarding self-energy insertions. The lower half of the energy plane, below the real axis, corresponds to the $[-, +]$ Riemann sheet standardly referred to as the second Riemann sheet and accessed from the physical region by crossing the real energy axis in between the $\pi\Sigma$ and $\bar{K}N$ thresholds. The upper half of the energy plane (above the real axis) shows the $[+, -]$ Riemann sheet, the third Riemann sheet, which does not allow for $\bar{K}N$ quasibound interpretation of poles located therein. The pole trajectories shown in the figure were calculated from the free-space pole positions (encircled dots) up to the pole positions at full nuclear density ρ_0. In addition to the two $I = 0$ poles listed and discussed in Table I of the

main text, each of the decoupled $\pi\Sigma$ and $\bar{K}N$ channels also exhibits an $I = 1$ pole, the one related to $\bar{K}N$ developing into a resonance residing on the $[+, -]$ Riemann sheet and another one related to a $\pi\Sigma$ state residing on the $[-, +]$ Riemann sheet. While the $I = 1$ pole related to $\pi\Sigma$ lies too far from the real energy axis to affect any physical observable, the one related to $\bar{K}N$ is responsible for the peak structure in the real part of the K^-n amplitude near threshold. However, the Riemann sheet location of this pole denies it of any quasibound interpretation. The $I = 1$ poles persist also in the more involved NLO chiral models discussed in Ref. [20].

As expected, the nuclear medium has no significant impact on the position of poles related to the $\pi\Sigma$ channel. On the other hand, both poles related to the $\bar{K}N$ channel move to considerably higher energies as the density increases. The $I = 0$ $\bar{K}N$ pole that affects most the $\bar{K}N$ scattering amplitude moves as high as about 1475 MeV, almost reaching the real energy axis. Since the pole is relatively far from the physical region due to the $\bar{K}N$ branch cut, the scattering amplitude exhibits a cusp instead of a proper resonance structure (see the dot-dashed line in Fig. 1 of the main text). When kaon self-energy is implemented the pole moves back below the $\bar{K}N$ threshold, residing now in the $[+, -]$ Riemann sheet. Since it remains relatively far from the physical region, one again gets a cusp structure as exhibited by the solid line in Fig. 1.

[1] Contributions to *Recent Advances in Strangeness Nuclear Physics*, edited by A. Gal and R. S. Hayano [Nucl. Phys. A **804** (2008)].

[2] W. Weise, Nucl. Phys. A **835**, 51 (2010), and references therein.

[3] D. Gazda, E. Friedman, A. Gal, and J. Mareš, Phys. Rev. C **76**, 055204 (2007); **77**, 045206 (2008); **80**, 035205 (2009).

[4] J. Schaffner-Bielich, S. Schramm, and H. Stöcker, in *Proceedings of the International School of Physics "Enrico Fermi", Course CLXVII*, edited by M. Anselmino *et al.* (IOS Press, Amsterdam, 2008), pp. 119–144; F. Özel, G. Baym, and T. Güver, Phys. Rev. D **82**, 101301(R) (2010).

[5] Y. Tomozawa, Nuovo Cimento A **46**, 707 (1966); S. Weinberg, Phys. Rev. Lett. **17**, 616 (1966).

[6] T. Waas, N. Kaiser, and W. Weise, Phys. Lett. B **365**, 12 (1996); **379**, 34 (1996).

[7] E. Friedman, A. Gal, and C. J. Batty, Phys. Lett. B **308**, 6 (1993); Nucl. Phys. A **579**, 518 (1994).

[8] E. Friedman, A. Gal, J. Mareš, and A. Cieplý, Phys. Rev. C **60**, 024314 (1999).

[9] J. Mareš, E. Friedman, and A. Gal, Nucl. Phys. A **770**, 84 (2006).

[10] E. Friedman and A. Gal, Phys. Rep. **452**, 89 (2007).

[11] Y. Akaishi and T. Yamazaki, Phys. Rev. C **65**, 044005 (2002); T. Yamazaki and Y. Akaishi, Phys. Lett. B **535**, 70 (2002).

[12] M. Agnello *et al.* (FINUDA Collaboration), Phys. Rev. Lett. **94**, 212303 (2005).

[13] T. Yamazaki *et al.* (DISTO Experiment), Phys. Rev. Lett. **104**, 132502 (2010).

[14] A. Ramos and E. Oset, Nucl. Phys. A **671**, 481 (2000).

[15] A. Cieplý, E. Friedman, A. Gal, and J. Mareš, Nucl. Phys. A **696**, 173 (2001).

[16] A. Cieplý, E. Friedman, A. Gal, D. Gazda, and J. Mareš, Phys. Lett. B **702**, 402 (2011).

[17] S. Wycech, Nucl. Phys. B **28**, 541 (1971).

[18] W. A. Bardeen and E. W. Torigoe, Phys. Lett. B **38**, 135 (1972).

[19] J. R. Rook, Nucl. Phys. A **249**, 466 (1975).

[20] A. Cieplý and J. Smejkal, Eur. Phys. J. A **43**, 191 (2010).

[21] M. Bazzi *et al.* (SIDDHARTA Collaboration), Phys. Lett. B **704**, 113 (2011), and references therein to previous experiments.

[22] N. Kaiser, P. B. Siegel, and W. Weise, Nucl. Phys. A **594**, 325 (1995).

[23] E. Oset and A. Ramos, Nucl. Phys. A **635**, 99 (1998).

[24] M. Lutz, Phys. Lett. B **426**, 12 (1998).

[25] A. D. Martin, Nucl. Phys. B **179**, 33 (1981), and references therein.

[26] U.-G. Meissner, U. Raha, and A. Rusetsky, Eur. Phys. J. C **35**, 349 (2004).

[27] D. Jido, J. A. Oller, E. Oset, A. Ramos, and U.-G. Meißner, Nucl. Phys. A **725**, 181 (2003).

[28] T. Hyodo and W. Weise, Phys. Rev. C **77**, 035204 (2008).

[29] N. Barnea and E. Friedman, Phys. Rev. C **75**, 022202(R) (2007).

[30] W. Weise and R. Härtle, Nucl. Phys. A **804**, 173 (2008).

[31] A. Trzcińska, J. Jastrzębski, P. Lubiński, F. J. Hartmann, R. Schmidt, T. von Egidy, and B. Kłos, Phys. Rev. Lett. **87**, 082501 (2001).

[32] A. Baca, C. García-Recio, and J. Nieves, Nucl. Phys. A **673**, 335 (2000).

[33] C. Vander Velde-Wilquet, J. Sacton, J. H. Wickens, D. N. Tovee, and D. H. Davis, Nuovo Cimento A **39**, 538 (1977), and references therein.

[34] M. Ericson and T. E. O. Ericson, Ann. Phys. (NY) **36**, 323 (1966). For a recent review see Ref. [10].

[35] J. K. Kim, Phys. Rev. Lett. **19**, 1074 (1967).